

# Plastic and low-cost zero thermal expansion alloy by a natural dual-phase composite

**Chengyi Yu**

Neutron Scattering Division, Oak Ridge National Laboratory, Oak Ridge, TN 37831

**Kun Lin**

University of Science and Technology Beijing

**Suihe Jiang**

University of Science and Technology Beijing <https://orcid.org/0000-0001-7749-1782>

**Yili Cao**

University of Science and Technology Beijing

**Wenjie Li**

University of Science and Technology Beijing

**Yilin Wang**

Beijing Advanced Innovation Center for Materials Genome Engineering, Institute of Solid State Chemistry, University of Science and Technology Beijing, Beijing 100083

**Yan Chen**

Oak Ridge National Laboratory

**Ke An**

Oak Ridge National Laboratory <https://orcid.org/0000-0002-6093-429X>

**Li You**

Beijing Advanced Innovation Center for Materials Genome Engineering, Institute of Solid State Chemistry, Department of Physical Chemistry, University of Science and Technology Beijing, Beijing 100083

**Kenichi Kato**

Japan Synchrotron Radiation Research Institute

**Qiang Li**

Beijing Advanced Innovation Center for Materials Genome Engineering, Institute of Solid State Chemistry, University of Science and Technology Beijing, Beijing 100083

**Jinxia Deng**

University of Science and Technology Beijing

**Xianran Xing** (✉ [xing@ustb.edu.cn](mailto:xing@ustb.edu.cn))

Beijing Advanced Innovation Center for Materials Genome Engineering, Institute of Solid State Chemistry, Department of Physical Chemistry, University of Science and Technology Beijing, Beijing 10008

## Article

**Keywords:** Zero thermal expansion, crystal structure, intermetallic compound, neutron diffraction, mechanical properties

**Posted Date:** January 13th, 2021

**DOI:** <https://doi.org/10.21203/rs.3.rs-138368/v1>

**License:**   This work is licensed under a Creative Commons Attribution 4.0 International License.  
[Read Full License](#)

---

**Version of Record:** A version of this preprint was published at Nature Communications on August 4th, 2021. See the published version at <https://doi.org/10.1038/s41467-021-25036-1>.

# Abstract

Zero thermal expansion (ZTE) alloys are not only of great scientific significance, but also of great application value due to their unique dimensional stability, high thermal and electrical conductivities. However, the practical application and further development of ZTE alloys are limited by their inherent brittleness because ZTE and plasticity are generally incompatible in a single material. Besides, ZTE alloy is highly sensitive to composition, so conventional methods such as alloying or the design of multiphase to improve its mechanical properties are inapplicable. In this study, we report a one-step eutectic reaction method to overcome this contradiction: by melting 4 atom% holmium with pure iron to form a natural dual-phase composite. The composite shows unprecedented comprehensive advantages such as moderate plasticity and strength, axial zero thermal expansion, good thermal stability and low cost, making it the first plastic ZTE alloy other than Invar. Through the joint study of synchronous X-ray diffraction, in-situ neutron diffraction and microscopy, the critical role of dual-phase synergy mechanism on both thermal expansion regulation and mechanical property enhancement is revealed. These results indicate that eutectic reaction is likely to be a general and effective method for the design of high-performance intermetallic compound-based ZTE alloys.

## Introduction

Zero thermal expansion (ZTE) alloy plays an important role in our daily life ranging from mechanical watches to communication satellites because of its size-stability under temperature fluctuations<sup>1-3</sup>. However, ZTE performance is rare in nature. This behavior is especially unusual for metallic materials: only a few couplings among lattice, spin and orbital induces a reduced coefficient of thermal expansion by virtue of the so-called magneto-volume effect<sup>4-6</sup>, which so far has been reported in conventional Invar alloy<sup>7</sup> ( $\text{Fe}_{0.64}\text{Ni}_{0.36}$ ) and some magnetic intermetallic compounds (e.g.,  $\text{Tb}(\text{Co,Fe})_2$ <sup>8</sup>,  $\text{La}(\text{Fe,Si,Co})_{13}$ <sup>9</sup>) among single-phase metallic materials. Unfortunately, most of these ZTE compounds are brittle with poor strength and little ductility<sup>10-14</sup>, giving rise to catastrophic fracture. By comparison, Invar is plastic and has become the only ZTE alloy that has been widely used, nevertheless it undergoes a low-strength and a high-cost. An alternative way to design ZTE alloys is mixing two components with opposite thermal expansions (e.g.,  $\text{La}(\text{Fe,Si})_{13}/\text{Cu}$ <sup>15</sup> and  $\text{ZrW}_2\text{O}_8/\text{Al}$ <sup>16</sup>). But these artificial composites usually suffer from undesirable microstructures or weak interfacial bonding, resulting in poor mechanical properties and thermal stability. More importantly, the magneto-volume effect is highly composition-sensitive – a slight interfacial mass transfer during high-temperature synthesis may suppress or vanish the ZTE property<sup>5, 13, 17</sup>. The search for novel ZTE alloys with excellent strength-plasticity combination remains challenging for decades<sup>18-22</sup>.

In this work, we employ a one-step strategy to design plastic and low-cost ZTE alloy by a hypo- or hyper-eutectic reaction in a binary system<sup>23-25</sup>. As we know, iron is one of the most earth-abundant elements; its conventional phase,  $\alpha\text{-Fe}$ , has high plasticity and normal positive thermal expansion (PTE). Interestingly, on the R-Fe (R = rare earth) binary phase diagram<sup>26</sup> (see Fig. S1), Fe forms a eutectic system

with  $R_2Fe_{17}$ , a typical negative thermal expansion (NTE) intermetallic compound driven by magnetic ordering<sup>6,27,28</sup>. This inspires us that the  $R_2Fe_{17}$  phase could coexist in equilibrium with Fe at any temperature without losing its own NTE character. What's more, both the phase fraction and microstructure can be easily controlled by tuning the chemical compositions in the binary system, which are key factors to thermal expansion and mechanical property regulations. Based on this guidance, we demonstrate that by adding only 4% Ho atoms to pure iron, a new alloy with both axial ZTE ( $Ho_{0.04}Fe_{0.96}$ ,  $\alpha_l = 0.19 \times 10^{-6} K^{-1}$ , 100 to 335 K) and the excellent strength-plasticity combination can be designed and fabricated. We further show that the present dual-phase alloy is highly stable under thermal circulation, which, to our best knowledge, is the first plastic ZTE alloy other than the Invar family and is cost-effective, and may hold great merit in potential applications.

## Results And Discussion

The targeted samples with compositions of  $Ho_xFe_{1-x}$  ( $x = 0.03, x = 0.04, x = 0.05, x = 0.07, x = 0.09$ , labeled as S-1 to S-5) were synthesized by traditional arc-melting methods. High-resolution synchrotron X-ray powder diffraction (SXRD) measurement was employed to identify the phase fractions and crystal structures. It shows that all the samples are dual-phase alloys consist of  $Ho_2Fe_{17}$  phase (denoted as **H**) and a iron phase (denoted as **a**) without other observable impurities (see Fig. 1a). Increasing the content of Ho atoms, the positions of Bragg peaks for both the **H** and **a** phases keep almost unchanged as indicated by  $(220)_H$  and  $(110)_a$  reflections in Fig. 1b, suggesting that the two phases reached thermodynamic equilibrium and can coexist in any proportion to ensure successful thermal expansion regulation. These results agree well with our expectations from the Ho-Fe binary phase diagram. Further Rietveld refinements quantified the phase fractions of the **H** phases ( $29.6 \pm 0.1\%$ ,  $39.8 \pm 0.1\%$ ,  $49.8 \pm 0.1\%$ ,  $69.7 \pm 0.2\%$  and  $86.5 \pm 0.3\%$  for S-1 to S-5, respectively, see Fig. 1c and Fig. S2).

Figure 1d shows the crystal structure of the **H** and **a** phases refined by SXRD data. The **H** phase adopts  $Th_2Ni_{17}$ -type structure (space group:  $P6_3/mmc$ ) with cell parameters  $a = 8.45 \pm 0.01 \text{ \AA}$ ,  $c = 8.32 \pm 0.01 \text{ \AA}$ ,  $V = 514.09 \pm 0.03 \text{ \AA}^3$  and has six Wyckoff sites ( $Ho_{2b}$ ,  $Ho_{2d}$ ,  $Fe_{4f}$ ,  $Fe_{6g}$ ,  $Fe_{12j}$  and  $Fe_{12k}$ ); while the **a** phase is a body-centered-cubic phase (space group:  $Im\bar{3}m$ ) with cell parameters  $a = 2.87 \pm 0.00 \text{ \AA}$ ,  $V = 23.56 \pm 0.02 \text{ \AA}^3$  and has only one Wyckoff site ( $Fe_{2a}$ ). Due to a large difference in atomic radius, Ho ( $1.79 \text{ \AA}$ ) and Fe ( $1.26 \text{ \AA}$ ) atoms occupy separate sites in the **H** phase selectively: Ho atoms are surrounded by Fe atoms and form  $[HoFe_{16}]$  cages (Fig. 1d). This guarantees the structural stability of the **H** phase when Fe atoms can diffuse through the interface during the high-temperature synthesis.

Electro-probe microanalyzer (EPMA) shows that the dendritic lamellar **a** phase (in dark, 50–100  $\mu\text{m}$ ) is homogeneously dispersed into the **H** phase (in white, 50–100  $\mu\text{m}$ ) matrix (see Fig. 2a-2e for S-2). Besides, the grain appears to grow along the loading direction (LD) (see Fig. 2b). Electron back-scattered diffraction (EBSD) inverse pole image demonstrates that the **H** and **a** phase are highly textured (Fig. 2e). To further investigate the lattice matching between the two phases in the bulk, neutron diffraction texture analysis was carried out. Neutron pole figures demonstrate a strong fiber texture in the as-cast sample:

the **H** phase is highly textured with the [008] axes parallel to the loading direction (LD) while the {600} zone axis perpendicular to LD; the **a** phase has a less-strong orientation with [110]<sub>a</sub> roughly parallel to LD (see Fig. 2d). Consequently, the main orientation relationship between **H** and **a** phase is [001]<sub>H</sub> // [110]<sub>a</sub>. This facilitates the formation of semi-coherent matching at the dual-phase interface, and will be discussed latter.

The hexagonal **H** compound shows NTE and is brittle, while the bcc **a** phase shows positive thermal expansion (PTE) and is plastic. Hence, both the coefficient of thermal expansion (CTE) and mechanical properties of the dual-phase alloys could be well controlled by adjusting phase content. Figure 3a indicates that the linear thermal expansion along LD of alloys can be successively tailored from moderate positive ( $\alpha_l = 2.7 \times 10^{-6} \text{ K}^{-1}$ , S-1) to strong negative ( $\alpha_l = -12.9 \times 10^{-6} \text{ K}^{-1}$ , S-5). Especially, an extraordinary axial ZTE over a wide temperature range (100 to 335 K) has been obtained in S-2 alloy ( $\alpha_l = 0.19 \times 10^{-6} \text{ K}^{-1}$ ). Due to the high texture in the alloys, the CTEs in-plane (TD - ND) from S-1 to S-5 are varied from  $7.7 \times 10^{-6} \text{ K}^{-1}$  to  $-0.1 \times 10^{-6} \text{ K}^{-1}$  (see Fig. 3b). Thereafter, the S-2 alloy containing Ho 4atm% is comprehensively characterized because of its ZTE behavior and morphological similarity to other samples. The lattice thermal expansions in the S-2 alloy were extracted by the temperature dependence of SXRD, which are  $9.40 \times 10^{-6} \text{ K}^{-1}$  for **a** phase along the *a* axis and  $-5.91 \times 10^{-6} \text{ K}^{-1}$  for **H** phase along the *c* axis (see Fig. S3 and Table 2). The apparent lattice thermal expansion along the  $Z_0$  direction of the alloy is  $0.92 \times 10^{-6} \text{ K}^{-1}$  (100-335K), consistent with that of dilatometer measurement (see Fig. 3c). What's more, S-2 displays good plasticity during compressive loading, as shown in the engineering stress-strain curve in Fig. 3d. The ultimate compressive stress ( $\delta_{US}$ ) is up to  $0.80 \pm 0.02 \text{ GPa}$  and the alloy undergoes almost 15.5% compressive strain with an obvious strain-hardening capacity before failure. To date, it has the best strength-plasticity combination performance other than the Invar family among all known ZTE or low thermal expansion (LTE) metallic materials.

To shed light on the mechanism for excellent strength and plasticity in the ZTE alloy, we investigated the co-deformation process of the two phases by in-situ neutron diffraction measurements under uniaxial compression<sup>29, 30</sup> (see Fig. S4). Two sets of neutron diffraction patterns were simultaneously recorded in the longitudinal direction (LD, along loading direction) and transverse direction (TD, perpendicular to loading direction) upon loading (see Fig. S5). The dramatic difference in peak intensities between LD and TD directions for both the **H** and the **a** phases is caused by fiber texture in the samples, in agreement with previous microstructure analysis (Fig. 4a and 4b). The lattice strain evolution with applied axial strains include three stages (see Fig. 4c): the soft **a** and brittle **H** phases co-deformed elastically in stage I; the **a** phase deformed plastically and the **H** phase still maintained elastically in stage II; eventually, co-deformed plastically in stage III.

Figure 4c demonstrates that the interplanar space of (004)<sub>H</sub> can be continuously compressed by increasing engineering strain up to 4.4%, corresponding to the elastic deformation of the **H** phase at stage II along with a gradually yielding of the **a** phase. We extracted the interaction between the soft **a** and the brittle **H** phases by illustrating the full width at half maximum (FWHM) of the reflections (Fig. 4d): the

slightly broadening of (110)<sub>L</sub> and (110)<sub>T</sub> in the **a** phase corresponds to dislocations generation during yielding (L and T represent LD and TD, respectively); however, the prominently broadening of (004)<sub>L</sub> in the **H** phase during elastic deformation corresponds to the accumulation of local strain gradient and the nucleation of shear bands. It should be emphasized that although both phases yielded and plastically deformed in stage III, the Th<sub>2</sub>Ni<sub>17</sub>-type **H** phase with large unit cell ( $V = 514.089 \pm 0.032 \text{ \AA}^3$ ) and low symmetry ( $P6_3/mmc$ ) lacks enough independent slip systems for plastic deformation. In fact, the plasticity of the **H** phase in State III is driven by the shear band mechanism<sup>21, 31, 32, 33, 34, 35</sup> (see Fig. S6). This is verified by the appearance of the splitting of the  $\{001\}_{\text{H}}$  reflections along with LD in this stage (arrows in Fig. 4a and Fig. S7)— there exist widespread lattice strains caused by shear bands. That is, the lamellar morphology from eutectic reaction enhances the alloys' mechanical performance via dual-phase synergistic interaction<sup>20, 23, 31, 36–39</sup>.

Phase interface also plays an important role in excellent mechanical behaviors and thermal stability<sup>40–42</sup>. High-resolution TEM reveals a  $\sim 1$  nm thick disordered transition layer at the interfaces as shown in Fig. 5a and 5b, two typical interfacial morphologies. The orientation relationship at these interfaces are  $\angle([110]_{\text{a}}, [001]_{\text{H}}) = 34.7^\circ$  and  $[112]_{\text{a}} // [001]_{\text{H}}$  (Fig. 5c and 5d), respectively, implying that there exist some extent of semi-coherent lattice matching between the two phases. The transition layers connect **H** and **a** phases via chemical bonding, minimalizing interfacial energy and giving rise to strong interface linkage and excellent thermal stability<sup>43, 44</sup>. Our thermal circulation test shows that the dual-phase ZTE alloys remain perfect integrity after hundreds of rapid switching between 77 K and 335 K (see Fig. S8). Besides, the high elastic strain energy of the brittle **H** phase can be effectively transferred to the soft **a** phase upon loading, and will be released via dislocation multiplication in the soft and plastic **a** phase. This improves the alloy's thermal stability and mechanic stability. Figure 5f demonstrates a typical shear band in **H** phase (along loading direction) after  $\sim 5\%$  deformation, where the lattice constant  $c$  near the shear band at region A (8.39 Å) is smaller than that away from it at region B (8.44 Å). The heterogeneous lattice strain in the **H** phase (see Fig. 5e–3 g) caused by interface interaction accounts for the splitting of the  $\{001\}_{\text{H}}$  reflections obtained by in situ neutron diffraction (Fig. 4a).

This dual-phase synergistic interaction mediated by interface was further demonstrated by ex-situ microstructure studies. After  $\sim 12\%$  deformation, the localized shear micro-cracks in the brittle **H** phase are inhibited by the soft **a** phase due to its lamellar structure (see Fig. S6). Hence, the **a** dendrites act as obstacles hindering the excessive deformation of the **H** phase by pinning the highly localized shear micro-cracks. Meanwhile, substantial dislocations generate in the plastic **a** phase after deformation to  $\sim 12\%$  strain (see Fig. S9), which eliminate the stress concentration of the hard **H** phase and make it plastic and robust. Further increasing strain, the micro-cracks divide into sub-micro-cracks along phase boundaries and lead to shear failure by the adjacent micro-crack penetration (See Fig. S10). These results illustrate that the dual-phase alloy undergoes large deformation by absorbing a large amount of fracture work, which improves the overall toughness and brings plasticity to the dual-phase alloy.

To assess the comprehensive properties of the S-2, we summarized our results in Fig. 6a, ultimate strain versus compressive strength and ZTE temperature range ( $\Delta T$ ) for the ZTE alloy (S-2), compared with other typical ZTE or near ZTE metallic materials<sup>5, 7, 8, 11, 12, 15, 18, 45–49</sup>. One can see that ZTE intermetallic compounds are of low-strength and high-brittleness though they possess desirable zero thermal expansion performance. To traditional La(Fe,Si)<sub>13</sub>-based composites, their strengths are high, but have little to no plasticity and the ZTE are mostly limited in a narrow temperature range. Er-Fe-V-Mo dual-phase alloy has high strength and wide near ZTE temperature window, but has no plasticity. In contrast, the present dual-phase ZTE alloy possesses a favorable strength-plasticity combination and a considerable wide ZTE temperature range ( $\Delta T = 235$  K) and is much stronger than the widely used Invar alloy at the comparable strain. Most importantly, this ZTE alloy is machinable and can be fabricated to various machine parts, such as precision gears against thermal shock and sealing ring enduring temperature fluctuation, etc., and is highly thermal stable (see Fig. 6b and Fig. S8). We also emphasize that the present ZTE alloy contains only 4 atm% rare-earth Ho with the rest component to be iron, which is a low-cost material with potential application prospect.

## Conclusion

In summary, we proposed a eutectic reaction method to overcome the contradiction between ZTE and plasticity in metallic materials. By this method, we successfully designed and fabricated a unique ZTE dual-phase alloy, Ho<sub>0.04</sub>Fe<sub>0.96</sub>, with a combination of low-cost, high thermal stability, and excellent strength-plasticity. The lamellar dual-phase microstructure with the semi-coherent interface not only regulates the thermal expansion behavior, but also greatly enhances the mechanical properties and improves the thermal stability of the ZTE alloy. The excellent comprehensive performance of the present dual-phase alloy may effectively avoid the "Buckets Effect" caused by the imbalance of material properties, endowing it a broad application prospect. We expect that more high-performance ZTE alloys could be explored using the eutectic reaction strategy.

## Methods

**Synthesis methods.** The samples of Ho<sub>x</sub>Fe<sub>1-x</sub> ( $x=0.03$ ,  $x=0.04$ ,  $x=0.05$ ,  $x=0.07$ ,  $x=0.09$ , labelled as S-1, S-2, S-3, S-4, S-5) were prepared the constituent elements, Ho and Fe (>99.9% purity) by a vacuum arc melting furnace under high purity argon atmosphere. The samples were turned over and melted four times to ensure homogeneity. Then, the sample was followed by annealing at 1373 K in an argon atmosphere for about 24 hours and quenched in water.

**SXRD measurements.** The ambient temperature and in-situ SXRD measurements of the samples were performed at the SPring-8 ( $\lambda = 0.45$  Å), Japan. The phase structures and fractions were obtained by Rietveld refinements with FULLPROF software.

**EPMA measurements.** The phase contrast and microstructure analysis were measured by electro-probe microanalyzer backscattering electron (EPMA-BSE) spectrum (SHIMADZU 1720) equipped with wave-

length dispersive spectrometer analysis (WDS) to quantitative determine the phase composition.

**SEM and EBSD measurements.** The surface of fracture and the microstructure orientation of the samples were measured by scanning electron microscope (SEM, Zeiss Geminisem 500), electron backscattering diffraction (EBSD, TESCAN MIRA 3 LMH SEM, and Symmetry EBSD).

**TEM measurements.** The microstructure of the as-cast sample was characterized by the high-resolution transmission electron microscopy (HRTEM) and was measured by an aberration-corrected FEI Titan G260–300 kV S/TEM. All pictures were handled with Gatan Digital Micrograph software.

**Apparent thermal expansion of the alloy.** The linear thermal expansion curves ( $\Delta l/l_0$ ) were measured by an advanced thermo-dilatometer (NETZSCH DIL402) with a heating rate of 5 K/min.

**Mechanical properties.** The sample was fabricated into  $\Phi$  6×8 mm cylinder by electrical discharging. At least 5 samples were tested for each composition. The room-temperature mechanical properties were measured using a CMT4105 universal electronic compressive testing machine with an initial strain rate of  $7.0 \times 10^{-4} \text{ s}^{-1}$ .

**In situ neutron diffraction measurements.** The real-time in-situ neutron diffraction experiments were carried out at VULCUM beamline in Oak Ridge National Laboratory (ORNL), USA. All the lattice strain during the compressive is determined by the single peak fitting method for the (h,k,l) reflections. The lattice strain was calculated by following formula

$$\text{Strain} = \frac{d_1 - d_0}{d_0} \times 100\%$$

Here  $d_1$  and  $d_0$  represent the interplanar crystal spacing of the (hkl) crystal plane after and before loading, respectively.

**The lattice thermal expansion of the dual-phase alloy.** The lattice thermal expansion of dual-phase alloy was calculated as:

$$\alpha_{s2} = \alpha_a \times \text{Len.}\%_{[a]} + \alpha_H \times \text{Len.}\%_{[H]}$$

where  $\alpha_a$  and  $\alpha_H$  are the CTEs along the  $c$  axis for **a** and **H** phase;  $\text{Len.}\%_{[a]}$  and  $\text{Len.}\%_{[H]}$  are length fractions of **a** and **H** along to  $c$  axis.

**Thermal cycling test.** To determine the thermal stability of the dual-phase alloys caused by the mismatch of CTEs between the two phases, a thermal-cycling test was conducted by switching the sample between 77 K and 335 K repeatedly. The thermal cycles test was conducted by an auto-mechanical arm. Put the

as-cast sample in liquid nitrogen (77 K) for 10 seconds and then transfer it to hot water (333 K) for 10 seconds, which is the whole cycle.

## Declarations

### DATA AVAILABILITY

The data that support the findings of this study are available from the corresponding authors upon reasonable request.

### COMPETING INTERESTS

The authors declare no competing interests.

### AUTHOR CONTRIBUTIONS

C.Y.Y. and K.L. designed the study. C.Y.Y. carried out the main experiments. C.Y.Y., K.L. and X.R.X. analyzed the data and wrote the main draft of the paper. S.H.J. analyzed the mechanical behavior of the sample. W.J.L., Y.L.C. and Y.L.W. analyzed the thermal expansion results. Y.C. and K.A. analyzed the in situ neutron diffraction results. L.Y. conducted the TEM characterization. K.K. conducted the SXRD measurements. All authors discussed the results and commented on the manuscript.

### ACKNOWLEDGEMENTS

This research was supported by National Natural Science Foundation of China (22090042 and 21731001, 21971009), National Key R&D Program of China (2020YFA0406200). The synchrotron radiation experiments were performed at the BL44B2 of SPring-8 with the approval of the Japan Synchrotron Radiation Research Institute (JASRI) (Proposal No. 2018B1306, 2018B1515); Neutron diffraction work was carried out at the Spallation Neutron Source (SNS) (Proposal No. 2019A21913, 2020B26069), which is the U.S. Department of Energy (DOE) user facility at the Oak Ridge National Laboratory, sponsored by the Scientific User Facilities Division, Office of Basic Energy Sciences. The authors thank Mr. M. J. Frost at SNS for the technique support.

## References

1. Mohn P. A century of zero expansion. *Nature* **400**, 18-19 (1999).
2. Zheng XG, Kubozono H, Yamada H, Kato K, Ishiwata Y, Xu CN. Giant negative thermal expansion in magnetic nanocrystals. *Nat Nanotechnol* **3**, 724-726 (2008).
3. Salvador JR, Guo F, Hogan T, Kanatzidis MG. Zero thermal expansion in YbGaGe due to an electronic valence transition. *Nature* **425**, 702 (2003).
4. Song Y, *et al.* Magnetic-Field-Induced Strong Negative Thermal Expansion in  $\text{La}(\text{Fe,Al})_{13}$ . *Chemistry of Materials*, (2020).

5. Hu J, *et al.* Adjustable Magnetic Phase Transition Inducing Unusual Zero Thermal Expansion in Cubic RCo<sub>2</sub>-Based Intermetallic Compounds (R = Rare Earth). *Inorganic Chemistry*, (2019).
6. Cao Y, *et al.* Role of “Dumbbell” Pairs of Fe in Spin Alignments and Negative Thermal Expansion of Lu<sub>2</sub>Fe<sub>17</sub>-Based Intermetallic Compounds. *Inorganic Chemistry*, (2020).
7. al MvSe. Origin of the Invar effect in iron-nickel alloys. *Nature* **400**, 4 (1999).
8. Song Y, *et al.* Zero Thermal Expansion in Magnetic and Metallic Tb(Co,Fe)<sub>2</sub> Intermetallic Compounds. *Journal of the American Chemical Society* **140**, 602-605 (2018).
9. Huang R, *et al.* Giant Negative Thermal Expansion in NaZn<sub>13</sub>-Type La(Fe, Si, Co)<sub>13</sub> Compounds. *Journal of the American Chemical Society* **135**, 11469-11472 (2013).
10. Hu J, *et al.* A case of multifunctional intermetallic compound: negative thermal expansion coupling with magnetocaloric effect in (Gd,Ho)(Co,Fe)<sub>2</sub>. *Inorganic Chemistry Frontiers*, (2019).
11. Dan S, Mukherjee S, Mazumdar C, Ranganathan R. Zero thermal expansion with high Curie temperature in Ho<sub>2</sub>Fe<sub>16</sub>Cr alloy. *RSC Advances* **6**, 94809-94814 (2016).
12. Zhao Y-Y, *et al.* Giant Negative Thermal Expansion in Bonded MnCoGe-Based Compounds with Ni<sub>2</sub>In-Type Hexagonal Structure. *Journal of the American Chemical Society* **137**, 1746-1749 (2015).
13. Li W, *et al.* Strong Coupling of Magnetism and Lattice Induces Near-Zero Thermal Expansion over Broad Temperature Windows in ErFe<sub>10</sub>V<sub>2-x</sub>Mo<sub>x</sub> Compounds. *CCS Chemistry*, 1009-1015 (2020).
14. Qing-Fang Guan S-HY, *et al.* Lightweight, tough, and sustainable cellulose nanofiber-derived bulk structural materials with low thermal expansion coefficient. *Science advances*, (2020).
15. Liu J, *et al.* Realization of zero thermal expansion in La(Fe,Si) 13 -based system with high mechanical stability. *Materials & Design* **148**, 71-77 (2018).
16. Wu G, Zhou C, Zhang Q, Pei R. Decomposition of ZrW<sub>2</sub>O<sub>8</sub> in Al matrix and the influence of heat treatment on ZrW<sub>2</sub>O<sub>8</sub> /Al-Si thermal expansion. *Scripta Materialia* **96**, 29-32 (2015).
17. Song Y, *et al.* Negative thermal expansion in (Sc,Ti)Fe<sub>2</sub> induced by unconventional magnetovolume effect. *Materials Horizons*, (2019).
18. Lin K, *et al.* High performance and low thermal expansion in Er-Fe-V-Mo dual-phase alloys. *Acta Materialia* **198**, 271-280 (2020).
19. Wang Y, *et al.* Enhanced thermal and mechanical properties of Sr<sub>0.2</sub>Ba<sub>0.8</sub>TiO<sub>3</sub>/Cu matrix composites by introducing Cu<sub>2</sub>O interface coating. *Materials & Design*, 107594 (2019).
20. Shi P, *et al.* Enhanced strength-ductility synergy in ultrafine-grained eutectic high-entropy alloys by inheriting microstructural lamellae. *Nat Commun* **10**, 489 (2019).
21. Wu G, Chan KC, Zhu L, Sun L, Lu J. Dual-phase nanostructuring as a route to high-strength magnesium alloys. *Nature* **545**, 80-83 (2017).
22. Takenaka K, Okamoto Y, Shinoda T, Katayama N, Sakai Y. Colossal negative thermal expansion in reduced layered ruthenate. *Nat Commun* **8**, 14102 (2017).

23. Pandey P, Makineni SK, Gault B, Chattopadhyay K. On the origin of a remarkable increase in the strength and stability of an Al rich Al-Ni eutectic alloy by Zr addition. *Acta Materialia* **170**, 205-217 (2019).
24. Sheng LY, Guo JT, Ye HQ. Microstructure and mechanical properties of NiAl–Cr(Mo)/Nb eutectic alloy prepared by injection-casting. *Materials & Design* **30**, 964-969 (2009).
25. Wang X, Leng H, Han B, Wang X, Hu B, Luo H. Solidified microstructures and elastic modulus of hypo-eutectic and hyper-eutectic TiB<sub>2</sub>-reinforced high-modulus steel. *Acta Materialia* **176**, 84-95 (2019).
26. O'KEEFE GJRATJ. The Fe-Ho Binary System. *Metallurgical Transactions* **1**, 3 (1970).
27. Cao Y, *et al.* Manipulating Spin Alignments of (Y,Lu)<sub>1.7</sub>Fe<sub>17</sub> Intermetallic Compounds via Unusual Thermal Pressure. *Inorg Chem* **59**, 5247-5251 (2020).
28. Cao Y, *et al.* Neutron Diffraction Study of Unusual Magnetic Behaviors in the Ho<sub>2</sub>Fe<sub>11</sub>Al<sub>6</sub> Intermetallic Compound. *Inorg Chem* **58**, 13742-13745 (2019).
29. An K, Skorpenske HD, Stoica AD, Ma D, Wang X-L, Cakmak E. First In Situ Lattice Strains Measurements Under Load at VULCAN. *Metallurgical and Materials Transactions A* **42**, 95-99 (2010).
30. Beese AM, Wang Z, Stoica AD, Ma D. Absence of dynamic strain aging in an additively manufactured nickel-base superalloy. *Nat Commun* **9**, 2083 (2018).
31. Ma Y, *et al.* Phase boundary segregation-induced strengthening and discontinuous yielding in ultrafine-grained duplex medium-Mn steels. *Acta Materialia* **200**, 389-403 (2020).
32. Jiang S, *et al.* Micromechanical behavior of multilayered Ti/Nb composites processed by accumulative roll bonding: An in-situ synchrotron X-ray diffraction investigation. *Acta Materialia*, 116546 (2020).
33. He G, Eckert J, Loser W, Schultz L. Novel Ti-base nanostructure-dendrite composite with enhanced plasticity. *Nat Mater* **2**, 33-37 (2003).
34. Inoue A, Shen B, Koshiba H, Kato H, Yavari AR. Cobalt-based bulk glassy alloy with ultrahigh strength and soft magnetic properties. *Nat Mater* **2**, 661-663 (2003).
35. Hofmann DC, *et al.* Designing metallic glass matrix composites with high toughness and tensile ductility. *Nature* **451**, 1085-1089 (2008).
36. Jin X, *et al.* A new CrFeNi<sub>2</sub>Al eutectic high entropy alloy system with excellent mechanical properties. *Journal of Alloys and Compounds* **770**, 655-661 (2019).
37. Su J, Raabe D, Li Z. Hierarchical microstructure design to tune the mechanical behavior of an interstitial TRIP-TWIP high-entropy alloy. *Acta Materialia* **163**, 40-54 (2019).
38. Bei H, George EP. Microstructures and mechanical properties of a directionally solidified NiAl–Mo eutectic alloy. *Acta Materialia* **53**, 69-77 (2005).
39. Kim SH, Kim H, Kim NJ. Brittle intermetallic compound makes ultrastrong low-density steel with large ductility. *Nature* **518**, 77-79 (2015).

40. Ran Ding<sup>1</sup> YY. Chemical boundary engineering: A new route toward lean, ultrastrong yet ductile steels. *science advances*, (2020).
41. K. Lu LL, S. Suresh. Strengthening Materials by Engineering Coherent Internal Boundaries at the Nanoscale. *Science* **324**, 4 (2009).
42. L. Lu XC, X. Huang, K. Lu. Revealing the Maximum Strength in Nanotwinned Copper. *Science* **323**, 4 (2009).
43. Sun L, Irving DL, Zikry MA, Brenner DW. First-principles investigation of the structure and synergistic chemical bonding of Ag and Mg at the Al| $\Omega$  interface in a Al–Cu–Mg–Ag alloy. *Acta Materialia* **57**, 3522-3528 (2009).
44. Liu J, Tennesen E, Miao J, Huang Y, Rondinelli JM, Heinz H. Understanding Chemical Bonding in Alloys and the Representation in Atomistic Simulations. *The Journal of Physical Chemistry C* **122**, 14996-15009 (2018).
45. Li S, Huang R, Zhao Y, Wang W, Han Y, Li L. Zero Thermal Expansion Achieved by an Electrolytic Hydriding Method in La(Fe,Si)<sub>13</sub> Compounds. *Advanced Functional Materials* **27**, 1604195 (2017).
46. Nakamura Y, Takenaka K, Kishimoto A, Takagi H. Mechanical Properties of Metallic Perovskite Mn<sub>3</sub>Cu<sub>0.5</sub>Ge<sub>0.5</sub>N:High-Stiffness Isotropic Negative Thermal Expansion Material. *Journal of the American Ceramic Society* **92**, 2999-3003 (2009).
47. Li LF, *et al.* Good comprehensive performance of Laves phase Hf<sub>1-x</sub>Ta<sub>x</sub>Fe<sub>2</sub> as negative thermal expansion materials. *Acta Materialia*, (2018).
48. Song Y, *et al.* Opposite Thermal Expansion in Isostructural Noncollinear Antiferromagnetic Compounds of Mn<sub>3</sub>A (A = Ge and Sn). *Chemistry of Materials*, (2018).
49. Wang J, *et al.* Balancing negative and positive thermal expansion effect in dual-phase La(Fe,Si)<sub>13</sub>/ $\alpha$ -Fe in-situ composite with improved compressive strength. *Journal of Alloys and Compounds* **769**, 233-238 (2018).

## Figures

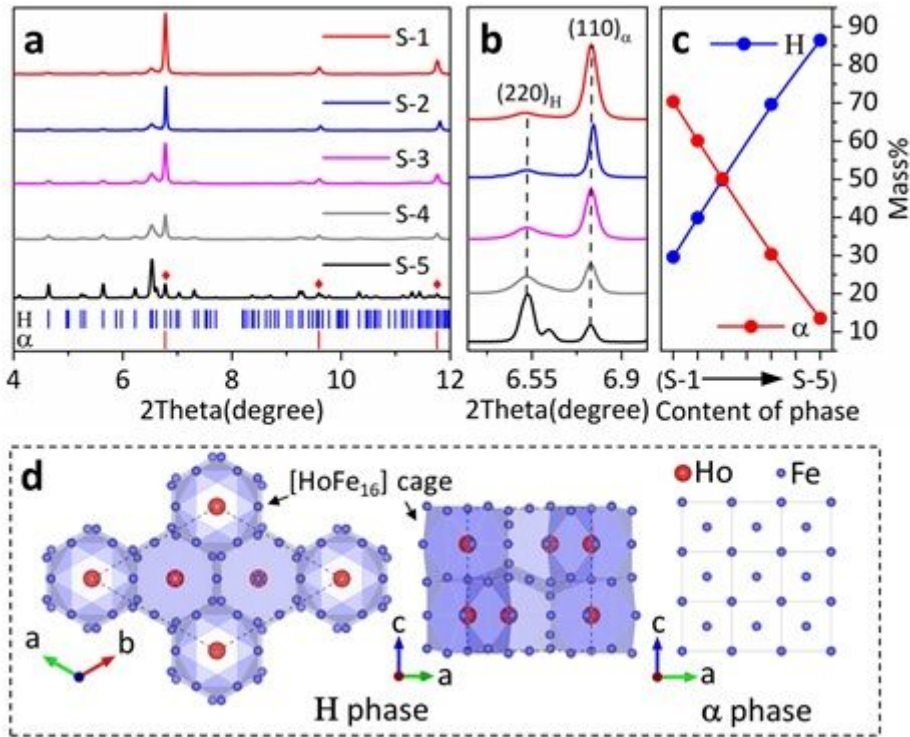


Figure 1

Phase and crystal structures. a, b High-resolution synchrotron X-ray diffraction profiles for S-1 to S-5 ( $\lambda = 0.23991 \text{ \AA}$ ). c The mass fractions of H and  $\alpha$  in S-1 to S-5 are determined via Rietveld refinements. d Crystal structures of H and  $\alpha$  phase, respectively.

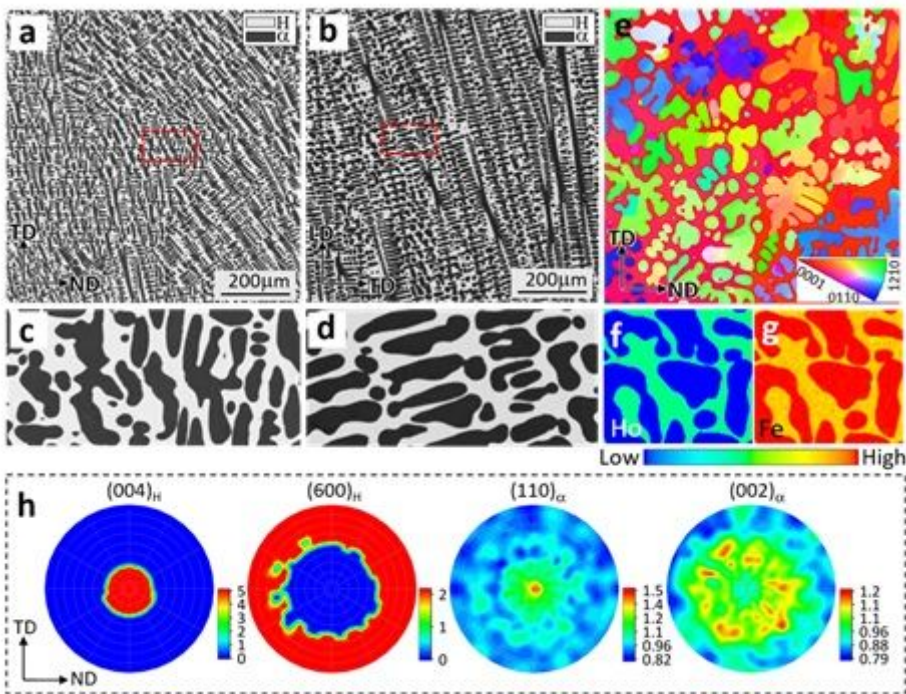
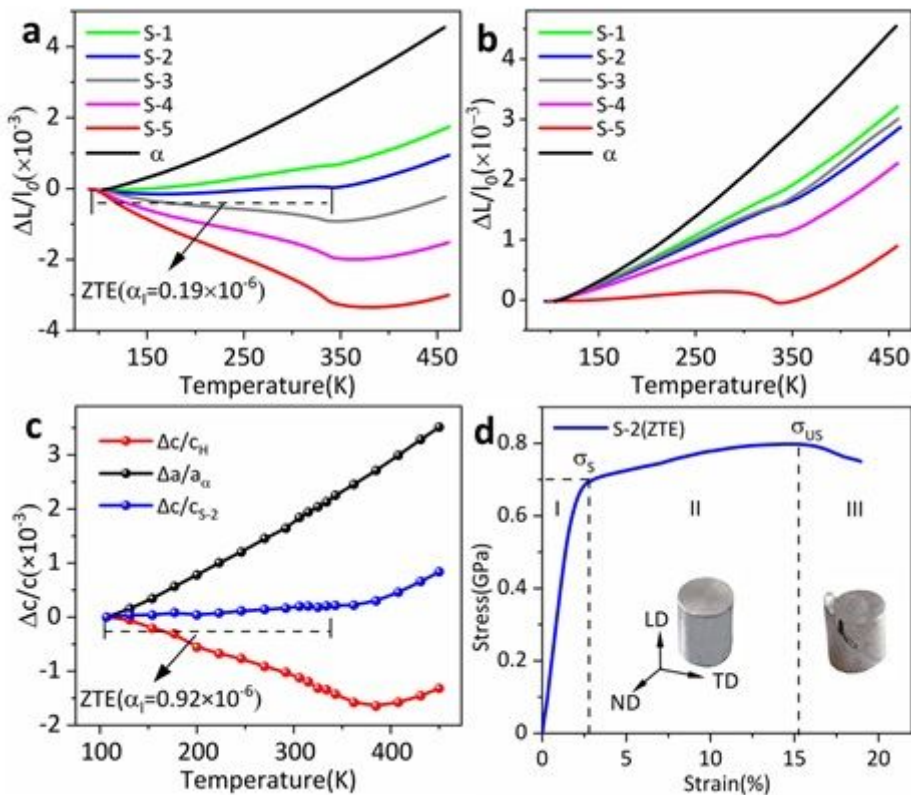


Figure 2

Microstructures of the ZTE alloy. a-d The morphology of the as-cast S-2 alloy confirmed by electro-probe microanalyzer (EPMA) in TD (transverse direction)-ND (normal direction) plane (a) and LD (loading direction)-TD plane (b), respectively. c and (d) are enlarged regions in (a) and (b). e Electron back-scattered diffraction (EBSD) inverse pole figure of crystal orientation for H phase inside the TD-ND plane. (f-g) Element mappings of Ho and Fe. h Pole figures by neutron diffraction texture analysis for the bulk orientations of (004)H, (600)H, (110)a, and (002)a directions.



**Figure 3**

Thermal expansion and mechanical properties. a Linear thermal expansions determined by advanced thermo-dilatometer for S-1 to S-5 and iron along with LD. b The in-plane (TD - ND) linear thermal expansion of S-1 to S-5 and iron. c Lattice thermal expansions of  $\alpha$  along the  $a$  axis, H along the  $c$  axis, and S-2 along with LD. d Compressive stress-strain curves of the S-2 with the insets of S-2 ingot during loading.

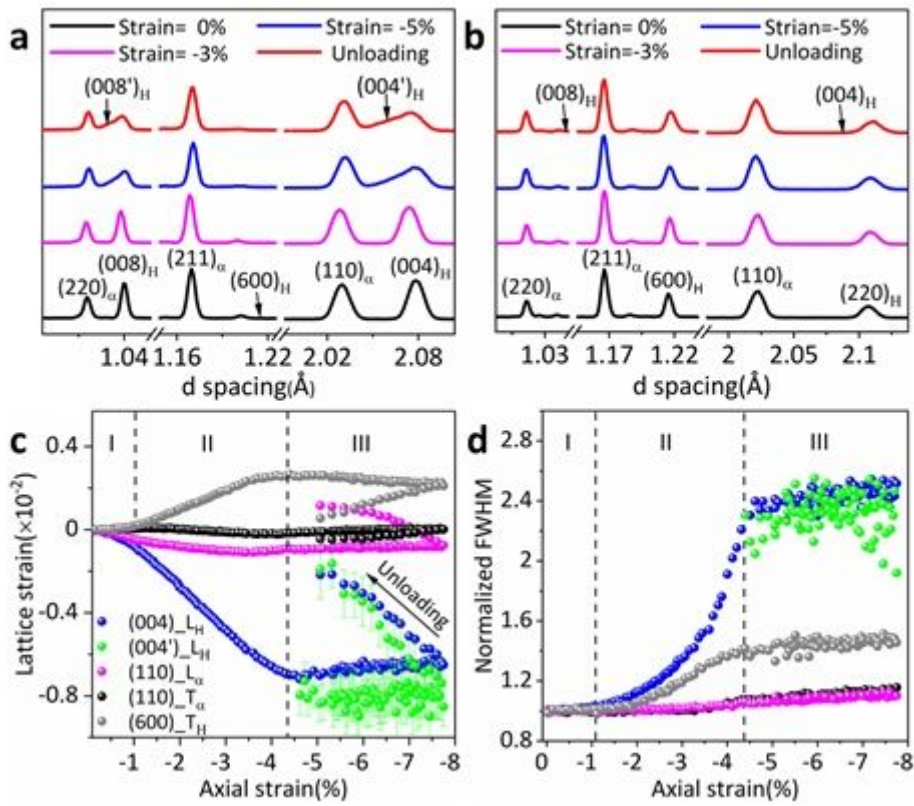


**Figure 4**

Real-time in-situ neutron diffraction studies. a, b In-situ neutron diffraction profiles at the strain of 0%, -3%, -5%, and unloading stage collected in the LD and TD, respectively, correspond to I, II and III stages. c, d Lattice strains and normalized peak FWHMs in LD and TD versus applied compressive strain, respectively.

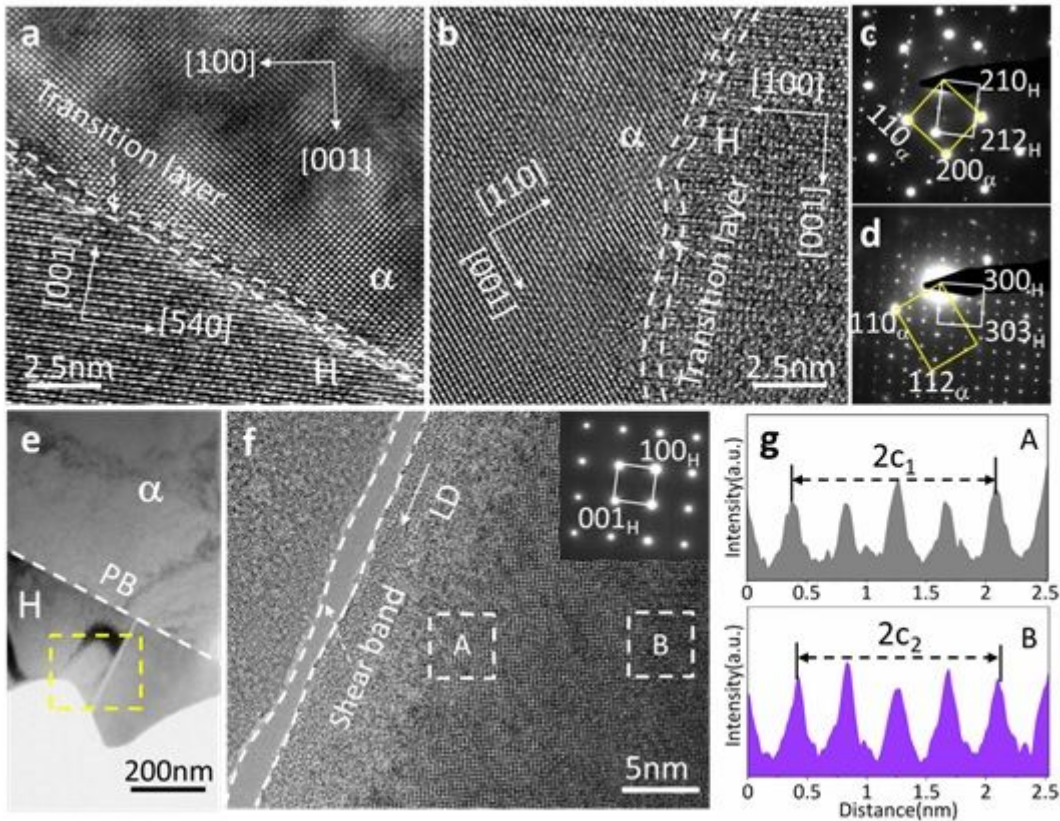


**Figure 5**

TEM studies. a, b High-resolution transmission electron microscopy (HRTEM) image at the phase interface, oriented to the  $[001]\alpha$  zone axis (a) and  $[11(-)0]\alpha$  zone axis (b), respectively. c, d Selected area electron diffraction (SAED) at the phase interface correspond to Fig. a and b, respectively. e The microstructure of the S-2 alloy at the strain of -5% along the loading direction. f The HRTEM image at the shear band area of the H phase, insert is the SAED at the H phase, oriented to the  $[010]$  zone axis. The local shear band is formed after large compressive deformation. g Intensity profile along with LD in A and B zones marked in Fig. 2f.

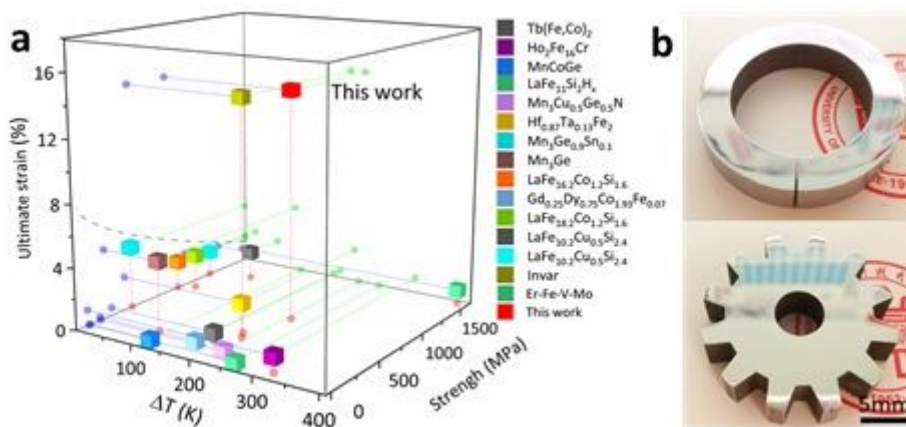


**Figure 6**

Summary of mechanical and thermal expansion performance. a A review of critical parameters for the typical (near) zero thermal expansion metallic materials: ultimate strain, strength, and temperature window. Note: Invar is a completely plastic material, for comparison, we used the compressive strength at 15.6% strains here. b Pictures of gear and sealing ring fabricated by the present ZTE alloy (S-2).

## Supplementary Files

This is a list of supplementary files associated with this preprint. Click to download.

- [SupportingInformation.docx](#)